Physics design of a 10 MeV injector test stand for an accelerator-driven subcritical system

Fang Yan,[1,*] Shilun Pei,[1] Huiping Geng,[1] Cai Meng,[1] Yaliang Zhao,[1] Biao Sun,[1] Peng Cheng,[1] Zheng Yang,[1,2] Huafu Ouyang,[1] Zhihui Li,[3] Jingyu Tang,[1] Jianli Wang,[1] Yefeng Sui,[1] Jianping Dai,[1] Peng Sha,[1] and Rui Ge[1]

[1]*Key Laboratory of Particle Acceleration Physics and Technology, Institute of High Energy Physics (IHEP), Chinese Academy of Science, Beijing 100049, China*
[2]*Department of Engineering Physics, Tsinghua University, Beijing 100084, China*
[3]*Institute of Nuclear Science and Technology, Sichuan University, Chengdu 610065, China*

(Received 2 November 2014; published 15 May 2015)

The 10 MeV accelerator-driven subcritical system (ADS) Injector I test stand at Institute of High Energy Physics (IHEP) is a testing facility dedicated to demonstrate one of the two injector design schemes [Injector Scheme-I, which works at 325 MHz], for the ADS project in China. The injector is composed of two parts, the linac part and the beam dump line. The former is designed on the basis of 325 MHz four-vane type copper structure radio frequency quadrupole and superconducting (SC) spoke cavities with $\beta = 0.12$. The latter is designed to transport the beam coming out of the SC section of the linac to the beam dump, where the beam transverse profile is fairly enlarged and unformed to simplify the beam target design. The SC section consists of two cryomodules with 14 $\beta = 0.12$ Spoke cavities, 14 solenoid and 14 BPMs in total. The first challenge in the physics design comes from the necessary space required for the cryomodule separation where the periodical lattice is destroyed at a relatively lower energy of ~5 MeV. Another challenge is the beam dump line design, as it will be the first beam dump line being built by using a step field magnet for the transverse beam expansion and uniformity in the world. This paper gives an overview of the physics design study together with the design principles and machine construction considerations. The results of an optimized design, fabrication status and end to end simulations including machine errors are presented.

DOI: 10.1103/PhysRevSTAB.18.054201 PACS numbers: 29.27.Bd, 29.27.Eg, 29.27.Fh, 41.75.Ak

I. INTRODUCTION

China ADS project is developing the concept and design of a 1.5 GeV high intensity superconducting (SC) linac with the aim of building a demonstration facility for the accelerator-driven subcritical system (ADS) in multiple phases lasting about 20 years. The driver linac will be operating in continuous wave (cw) mode and delivering 15 MW beam power eventually. The general layout of the linac is shown in Fig. 1. The linac includes two major sections: the injector section and the main linac section. The injectors accelerate the proton beams up to 10 MeV and the main linac boosts the energy from 10 MeV up to 1.5 GeV.

To satisfy the restricted stability and reliability command [1] of the linac in the lower energy part, there will be two identical injectors operating paralleled backing up for each other. At present, two different design schemes for the injectors are proposed [2,3], with scheme I (so-called Injector I) based on 325 MHz (the same frequency with the main linac) and scheme II (so-called Injector II) based on 162.5 MHz. Finally only one scheme will be chosen and two identical injectors will be built and operated as a hot spare stand-by.

In the first stage, two 10 MeV test stands will be fabricated independently in two institutes: IMP (Institute of Modern Physics) and IHEP, based on two different injector design schemes. For both design schemes, the injector is composed of an electron cyclotron resonance (ECR) ion source, a low energy beam transport (LEBT) line, a four-vane type copper structure radio frequency quadrupole (RFQ), a medium energy beam transport (MEBT) line and a superconducting (SC) section. There will be a matching section—MEBT2 [4] to transfer the beam from any of the two injectors to the main linac. In the test stand, the MEBT2 section is replaced by a beam dump line for transporting the proton beam out of the SC segment to the beam dump.

This paper will focus on the test facility design basing on the Injector I scheme. The detailed design of the main linac can be found in Ref. [5]. The paper gives an overview of the physics design study of the IHEP 10 MeV testing facility together with the design principles and machine construction considerations. The results of an optimized design, fabrication status and end to end simulations including machine errors are presented.

*yanfang@ihep.ac.cn

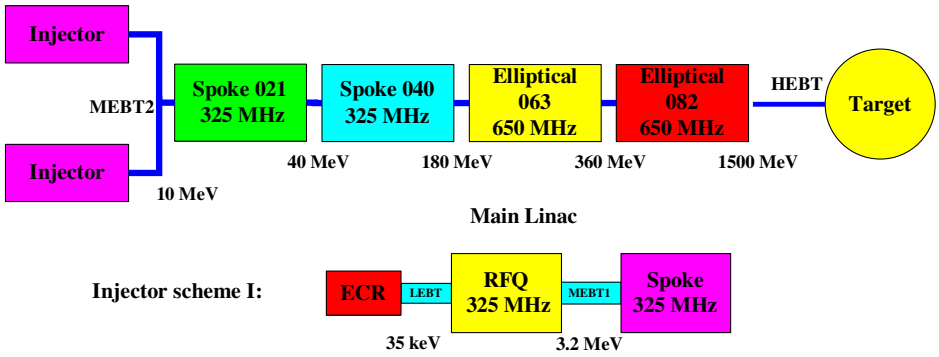

FIG. 1. The general layout of the ADS linac in China.

II. SPACE CHARGE INSTABILITY AND BEAM HALO CONTROL

The design philosophy and consideration of this paper are mainly focused on the beam loss controlling by avoiding the instability resonances during the design. Other design considerations are covered in another paper [6]. The utmost design goal of a high intensity linac is controlling the beam loss along the linac as low as possible. The common acceptance of the beam loss rate is 1 W/m considering hands-on maintenance. The higher the final beam power is, the more challenging to realize it. For the China ADS project, the designed beam power on target is 15 MW, this means that the particle loss rate has to be controlled down to the magnitude of 1×10^{-8}/m at the high energy part. However, most of the beam loss in this level could be traced to the instable or sensitive design in the low energy section. For periodic accelerating structures, the instabilities of the beam driven by the periodic-focusing lattice and mismatch oscillations of the beam could be summarized as the longitudinal parametric resonances and transverse structure resonances. To avoid these resonances, general practice for conservative design is to limit the external focusing strength so that $\sigma_0 < 90$ degrees in all three planes [7]. However, this longitudinal constrain limits the accelerating gradient of the high-gradient SC linac, especially at the low energy section. If it could be relaxed to some extent, the accelerator cost could be saved. But the realistic question is to what extent it could be relaxed and it surely has close association with the space charge force of the beam. The space charge effect in the beam is characterized by the tune depression. The detailed deduction of the tune depression refers to citation [7] and it is concluded here for easy reference.

A. Tune depression

The transverse tune depression equation [(4.99) of Ref. (7)] for a round matched beam under smooth approximation is formulated in the following:

$$\eta_t = k_t/k_{t0} = \sqrt{1+u^2} - u, \tag{2.1}$$

where the wave numbers k_t and k_{t0} represent the transverse focusing forces acting on the particles with and without space charge effect, respectively. The dimensionless parameter u is defined as

$$u = K_t/2k_{t0}\varepsilon_t. \tag{2.2}$$

Here, the transverse focusing forces acting on the particles are represented by the wave number $k_{t0} = \sigma_{0t}/L$ and σ_{0t} is the transverse zero current phase advance of the "betatron" oscillation per focusing period of length L. The transverse emittance is represented by $\varepsilon_t = 4\varepsilon_{n.rms.t}/\beta_0\gamma_0$, $\varepsilon_{n.rms.t}$ is the normalized rms emittance. $\beta_0 = v_0/c$, $\gamma_0 = (1-\beta_0{}^2)^{-1/2}$ are the relativistic velocity and energy factor, v_0 is the centroid velocity, c is the speed of light. The generalized transverse perveance parameter K_t is defined as follows:

$$K_t = \frac{3}{2}\frac{Nr_c}{\beta_0^2\gamma_0^3}\frac{1}{z_m}\left(1 - \frac{g}{2}\frac{a^2}{\gamma_0^2 z_m^2}\right). \tag{2.3}$$

Here, N is the number of particles in the bunch, related to the average beam current I by $N = I\lambda/qc$, λ is the wavelength of the rf field in the accelerating structure of the rf linac, and q is the particle charge. The classical particle radius $r_c = q^2/4\pi\varepsilon_0 mc^2 = 1.5347 \times 10^{-18}$ m for proton and ε_0 is the permittivity of free space. If the ratio of the beam radius a and half length z_m of the bunch are equal or smaller than $4(\gamma_0/z_m \le 4)$ and the tube radius is significantly larger than the beam radius (say $b/a \ge 5$), thus the geometry factor can be approximated by $g = g_0 \approx 2\gamma z_m/3a$ while a and z_m are approximated by

$$a = \left[\left(\frac{3}{2}\right)^2 \frac{Nr_c}{\beta_0^2\gamma_0^2}\frac{1}{k_{l0}^2}\left(\frac{k_{t0}^2}{k_{l0}^2} + \frac{1}{2}\right)^{-2} + \left(\frac{\varepsilon_{nt}}{\beta_0\gamma_0 k_{t0}}\right)^{3/2}\right]^{1/3}, \tag{2.4}$$

$$z_m = \left[\frac{2}{3}\frac{Nr_c}{\beta_0^2\gamma_0^5}\frac{1}{k_{l0}^2}\left(\frac{k_{t0}^2}{k_{l0}^2} + \frac{1}{2}\right) + \left(\frac{\varepsilon_{nl}}{\beta_0\gamma_0 k_{l0}}\right)^{3/2}\right]^{1/3}. \tag{2.5}$$

Here, the transverse and longitudinal normalized emittance are $\varepsilon_{nt} = 4\varepsilon_{n.rms.t}$ and $\varepsilon_{nl} = 4\varepsilon_{n.rms.z}$, respectively. k_l and k_{l0} are the longitudinal wave numbers with and without space charge.

Longitudinally, the tune depression is represented by

$$\eta_l = \frac{k_l}{k_{l0}} = \left(1 + \frac{K_L z_m}{\varepsilon_{zz'}^2}\right)^{-1/2}. \tag{2.6}$$

Here, the longitudinal emittance $\varepsilon_{zz'} = 4\varepsilon_{n.rms.z}/\beta_0\gamma_0{}^3$ and the longitudinal perveance parameter is represented by

$$K_L = \frac{3}{2}\frac{gNr_c}{\beta_0^2\gamma_0^5}. \tag{2.7}$$

B. Parametric resonance and longitudinal instability

One important parametric resonance occurs when the phase advance per period of the envelope mismatch oscillation fulfills the condition: $k_{mm}L = \pi$, k_{mm} is longitudinal wave number of the envelope mismatch oscillation period, which is associated with the single particle longitudinal wave number by the following equation [8]:

$$k_{\ell 0} = k_{mm}\Big/\sqrt{1 + 3\eta_l{}^2} = \pi/L\Big/\sqrt{1 + 3\eta_l{}^2}. \tag{2.8}$$

Plugging in the longitudinal tune depression, the longitudinal zero current phase advance on resonance could be obtained by this equation. The resonance occurs at this particular point; technically to avoid the instability $k_{\ell 0}$ could be smaller or bigger. But if starting with bigger $k_{\ell 0}$, the resonance may satisfy when $k_{\ell 0}$ falls off as the longitudinal phase advance decreases rapidly with increasing β, so that the resonant point puts an upper limit for the longitudinal zero current phase advance.

For the low energy SC lattice, one focusing of period includes not only the cavity but also the transverse focusing devices and necessary spaces for accommodating these optics such as the helium tank, tuner, and other necessary accessories. The longitudinal instability is also associated with the so-called filling factor $F = l_{\text{eff}}/L$, defined by the ratio of the longitudinal effective length l_{eff} and the focusing period length L. The width of the unstable region is described by the following equation with the center of the first unstable region $\sigma_{l0} = \pi$ [9]:

$$\varepsilon = \frac{\sigma_{l0}}{2}\frac{\sin(\pi l_{\text{eff}}/L)}{\pi l_{\text{eff}}/L}. \tag{2.9}$$

This formula puts a more strict constrain on the longitudinal phase advance if the longitudinal filling factor is relatively small. Once the longitudinal phase advance constrain is obtained, the accelerating gradient can only be lifted by shortening the focusing period length and reducing the magnitude of cavity synchronous phase while keeping enough longitudinal acceptance.

C. Transverse instability

Systematic and self-consistent theoretical study showed the transverse instability stop bands named breathing mode, quadrupole mode and sextupole mode *et al.* according to their azimuthal symmetry. The resonant conditions of the breathing mode (σ_+) and quadrupole mode (σ_-) are described as follows [10]:

$$\sigma_+ = \sqrt{2\sigma_{0t}^2 + 2\sigma_t^2} = 180°, \tag{2.10}$$

$$\sigma_- = \sqrt{\sigma_{0t}^2 + 3\sigma_t^2} = 180°. \tag{2.11}$$

For practical applications, the stop bands are also sensitive to the solenoid occupancy $F_t = l_{t.\text{eff}}/L$ ($l_{t.\text{eff}}$ is the transverse effective length). The instability bands get wider and mode growth rates stronger with decreasing F_t. Taking account of the solenoid filling factor, these formulas were revised by correction factors as shown in Eqs. (80)–(84) of Ref. [10]. However, the formulas above could still be used to roughly predict band locations. Among all these pure transverse modes, the most prominent case resulting from the theoretical study has been the so-called envelope instability (quadrupole mode). Its existence was studied experimentally in a linear transport experiment at LBNL [11].

Recently, experiments indicated that the fourth order resonance (octupole mode) dominates over the envelope instability when approaching the resonant condition: $4\sigma_t = 360°$ (so-called 90° stop band) [12,13]. The resonant was found for $\sigma_t \approx 85°$ while $\sigma_{0t} \approx 100°$ with tune depression of 0.85. The transverse instability constrain also put an upper limit to the transverse zero current phase advance according to the lower boundary of the solenoid mode band as the transverse phase advances have to be varied versus the longitudinal phase advance to ensure the working points of the linac confined in stable area to avoid transverse and longitudinal coupling.

D. Transverse and longitudinal coupling resonance

One important beam dynamics resonant condition coupling the longitudinal and transverse motion is the $k_l = 2k_t$ resonance. Analysis of the coupling effect showed substantial amplitude and emittance growth [8]. This resonance is more severe in the low energy part but could be easily avoided by shifting the tune print of the working point away from the resonant area. Further analyses show also other anisotropy instabilities identified by $k_l/k_t = 1/3,\ 1/2,\ 1$ and 2 which lead to emittance transfer between transverse and longitudinal degrees of freedoms [14]. If the beam is space charge dominated: $Nr_c a/\varepsilon_{nt}^2 \gg 1$, these effects could be avoided by thermal equilibrium design through the condition of [15]:

$$\frac{k_{t0}}{k_{l0}} = \left(\frac{3\varepsilon_{nl}}{2\varepsilon_{nx}} - \frac{1}{2}\right)^{1/2}. \tag{2.12}$$

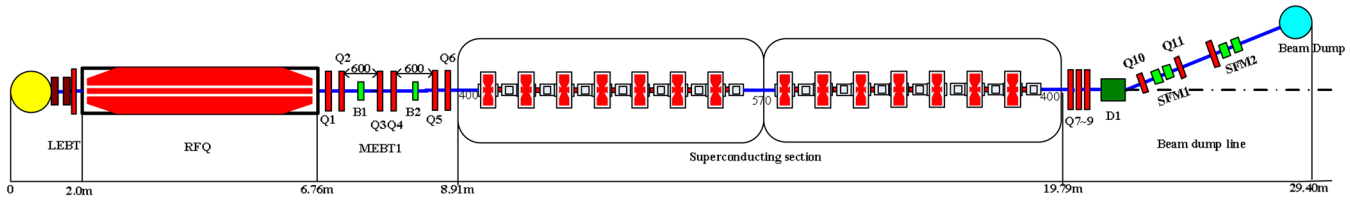

FIG. 2. The schematic layout of the 10 MeV test stand in IHEP.

Study shows that stable conditions also exist for the nonequipartitioned beams in relatively large regions of parameter space and stable design can be achieved by choosing the working points in the stable area or quickly passing by the stop band near $1/3$, $1/2$, and 1 on the Hofmann stability chart [16], in which $k_l/k_t = 1$ is the most severe. These stop bands are not always present. The degree of strength of the resonance peak varies according to the change of the transverse and longitudinal emittance ratio and the $k_l/k_t = 1$ resonance is suppressed if the emittance ratio is near to unity.

III. PHYSICS DESIGN AND FABIRICATION STATUS OF DIFFERENT SECTIONS

The schematic layout of the 10 MeV Injector I test stand in IHEP is presented in Fig. 2. The 35 keV proton beam from the ion source is bunched and accelerated to 3.2 MeV by a 325 MHz RFQ. The LEBT undertakes the matching between the source and RFQ and also provides chopped beam for commissioning. The SC section accelerates beam from 3.2 MeV up to 10 MeV employing Spoke cavities with the same frequency. The beam dump line follows right after the SC segment. Two pair of step field magnets (SFM) are adopted for transverse beam expanding and uniformities.

A. Ion sources and LEBTs

To ensure the beam quality in RFQ, the energy deviation and the beam current stability at the entrance of the RFQ are requested to be smaller than 0.1% and ±1%, respectively [17]. The ADS linac will be operating in cw mode. But the pulsed beam is an essential choice for the beam tuning stage. The front end needs to have the ability to provide adjustable

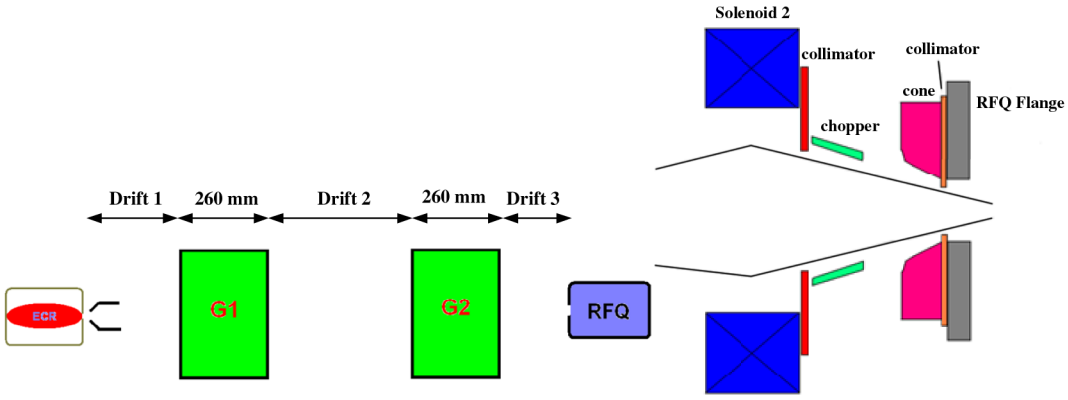

FIG. 3. The schematic figure of the LEBT (left) and chopper (right). G1 and G2 are for Glaser magnetic lenses.

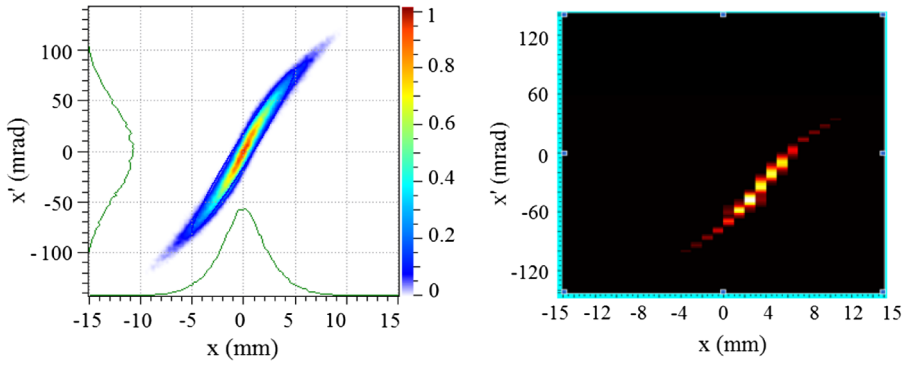

FIG. 4. Beam phase space at the measured location (8.8 cm drift downstream of the LEBT exit): simulation results (left) and measurement results (right).

TABLE I. The measurements versus the design goal of the beam current, Twiss parameters and normalized RMS emittance at the exit of the LEBT.

Parameters	I_{beam} (mA)	α	β (mm/mrad)	$\varepsilon_{n.rms.t}$ (π mm.mrad)
Design goal	10	2.41	0.0771	<0.20
Measurement (backward deduced from the measured location)	11.5	2.18	0.0774	0.14

beam. 30 μs to cw continuously adjustable beam is achieved with a fast rise/fall time of smaller than 20 ns [18]. The schematic figure of the LEBT and chopper is shown in Fig. 3. The difficulty of the LEBT is to control the emittance growth and reach an efficient transport, especially for high intensity beam. So that the LEBT is designed to be as short as possible, the total length is 1.67 m. The ion source, LEBT and RFQ had been installed in the experiment hall in IHEP. The beam out of LEBT was tested and the basic parameters were measured. Figure 4 shows the beam horizontal phase space 8.8 cm downstream of the LEBT exit. The measurement (right) and the design (left) is quite close except the position of the beam shifted. Table I presented the measurement of the beam current, Twiss parameters and normalized RMS emittance and the corresponding design value of each parameter, from which we could conclude that the design can fulfill the requirements.

B. RFQ

While operating on cw mode, the biggest issue of the copper structure RFQ is the power dissipation. 162.5 MHz frequency choice benefits for smaller surface power density because of half frequency and twice bigger size. But the drawback originates also from the big size for the accuracy control difficulty of the fabrication and welding along with the big deformation after welding. The advantage of the 325 MHz choice is the smaller size, but much more attention has to be paid on the cooling system. IHEP selected the 325 MHz RFQ eventually. One reason is that the 325 MHz is close to the previously developed RFQ (352 MHz) in IHEP for ADS studies. Although the duty factor of this former developed RFQ had been pushed to 7% [19] maximum, the fabrication and commissioning experiences could still be valuable. Another reason is that if 162.5 MHz is selected, there will be a frequency jump at 10 MeV. It could be a source for halo development as matched beam is hard to be achieved with strong space charge effect at the low energy part where the periodical lattice is discontinued, and the situation would be worse if there is a frequency jump.

TABLE II. The main parameters of the 10 MeV test stand RFQ in IHEP.

Parameters	RFQ in IHEP
rf frequency (MHz)	325.0
Pulsed beam current (mA)	15
Injection energy (keV)	35
Output energy (MeV)	3.2
Intervane voltage (kV)	55
Minimum aperture (mm)	2
Maximum modulation	2
Accelerator length (cm)	469.95
$\varepsilon_{n.rms.t}$(π mm mrad)	0.2
$\varepsilon_{n.rms.l}$(π mm mrad/π deg MeV)	0.16/0.058

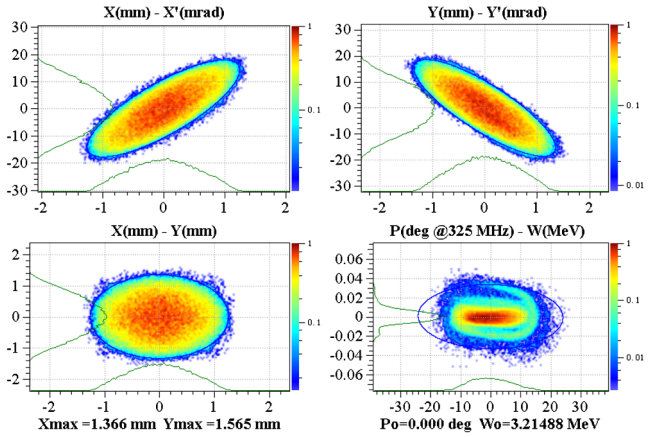

FIG. 5. The RFQ simulated output phase space exit [20].

The main parameters of the RFQ are listed on Table II. The total accelerator length of the RFQ is 4.7 m. It is composed of two resonantly coupled physical segments and each segment includes two technical modules connected together with flanges. The length of each technical module is limited to 1.2 m by the machine capability in industry domestically based on the construction experience of the previous RFQ [19] built at IHEP for ADS studies. The longitudinal normalized rms emittance is designed to be smaller than transverse emittance for better cavity efficiency.

The beam dynamics of the RFQ is carried out by the PARMTEQ program. 4D water-bag distribution with 100,000 macroparticles are assumed for the initial distribution. The output phase space is presented in Fig. 5. The simulated RFQ output distribution has been used for the

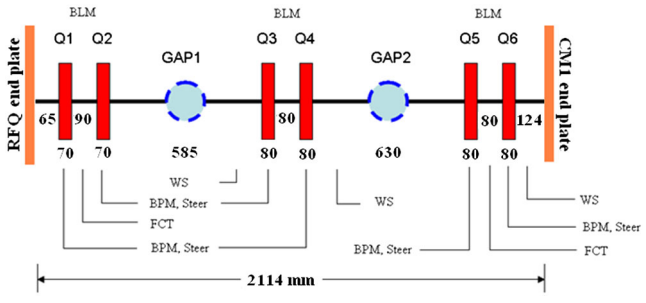

FIG. 6. The schematic of Injector I MEBT.

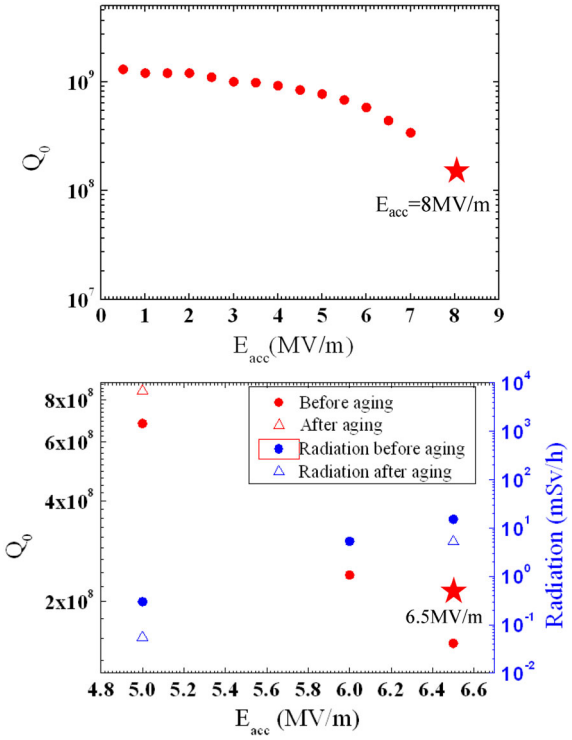

FIG. 7. Test results of the first prototype Spoke012 cavities: vertical test @2012.12.24 (above) horizontal test @2013.09.16 (below).

design of the SC linac. At present, the RFQ is under conditioning and 90% duty factor has been achieved with 92% beam transmission from the entrance of RFQ to the exit [20].

C. MEBT

The MEBT are composed of six quadruples, six steering magnets and two bunchers as shown in Fig. 6. The quadruples are used to provide smooth transportation from RFQ to the SC section while the bunchers are used for the longitudinal matching. The first buncher is very critical and it is demanded to capture and bunch the beam to the second buncher position with RMS phase spread smaller than 12 degrees to keep the beam in the linear region of the buncher field. Beam diagnostic devices including six beam position monitors, three beam loss monitors, two fast current transformers and three wire scanners which are planted in between the quadruples to measure the beam positions and transportation. No collimators are considered in this transfer line as it was believed that the transverse beam is relatively clean out of RFQ and longitudinal beam halos cannot be collimated unless in the bend section.

D. Superconducting linac of the Injector I

The 325 MHz SC $\beta = 0.12$ single spoke cavity (Spoke012) is selected for the acceleration from

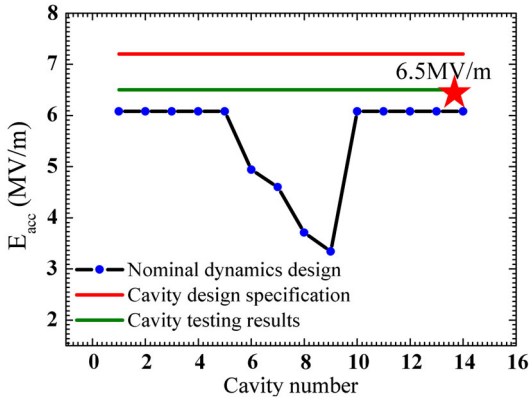

FIG. 8. The E_{acc} specifications (red line), the horizontal testing results (green line) and the current design (dotted line) of the Spoke012 cavities.

3.2 MeV up to 10 MeV. This is the first spoke cavity in the world for such low beta design. The fabrications of the first five cavities have been completed and the horizontal tests were successfully performed for the first two prototype cavities [21]. The accelerating gradient of $E_{acc} = 6.5$ MV/m had been achieved during the horizontal test in Sep. 16, 2013 as shown in Fig. 7 (below). The physics design had been adjusted according to the testing results. As shown in Fig. 8, the red line was the former accelerating gradient specifications of the Spoke012 cavity, the green line is the testing results and the dotted line is the current

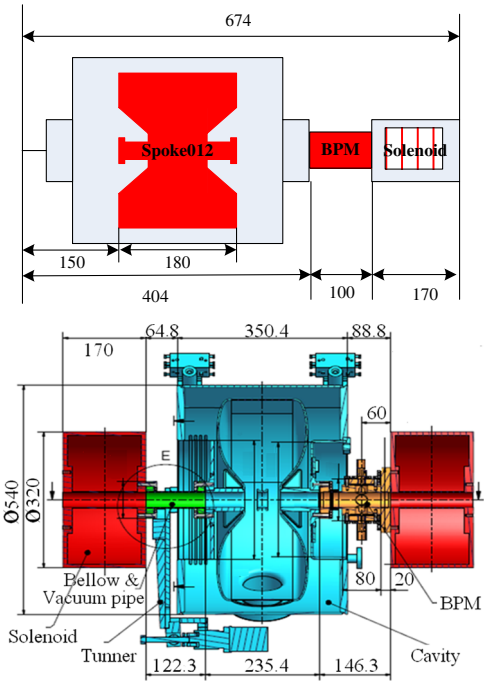

FIG. 9. The lattice structure of the Spoke012 section: physics design (above), mechanical design (below).

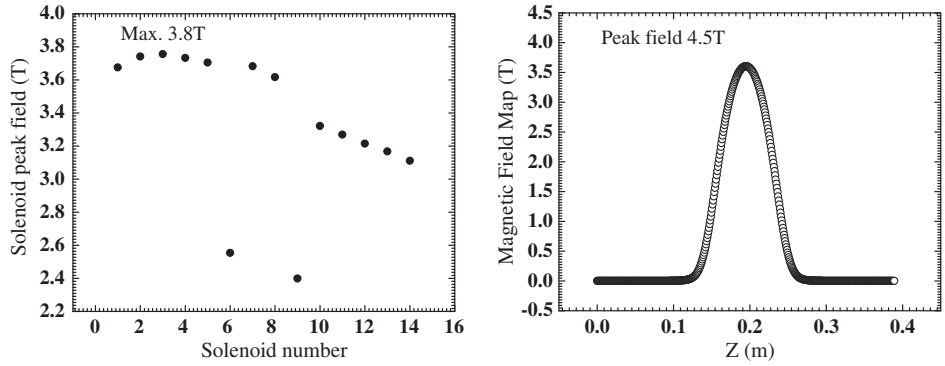

FIG. 10. The peak fields of the solenoids along the SC section of Injector I (left) and the designed field extension of the solenoid (right).

design. A conservative design is adopted to ensure the success of the project progress but with the cost of two more cavities.

1. Lattice design

The ADS Injector I period length of the SC section lattice is 0.674 m as shown in Fig. 9 (above graph). One focusing period of Spoke012 section consists of one Spoke012 cavity, one SC solenoid and one Beam position monitor (BPM). The mechanical length of the cavity from flange to flange is 404 mm as shown in Fig. 9 (upper graph). Noteworthy, the cavity is not in the center of the helium jacket but shifted 38 mm upstream for tuner installation convenience. The solenoid designed peak field is 4.5 T as presented in Fig. 10 (right). The maximum peak field in use is 3.8 T as shown in Fig. 10 (left). 15% margin is remained in case the matching between cryomodules needs more gradient.

According to the tune depression equations presented in Sec. II A, the transverse and longitudinal tune depressions at the entrance of the SC section are 0.64 and 0.67, respectively. They remain almost constant along the injector section. Plugging the longitudinal tune depression in Eq. (2.8), we get the resonant condition of $\sigma_{0l} = k_{\ell 0}L = 118°$. According to this constrain, the longitudinal zero current phase advance is necessarily kept below 118° to avoid the envelope mismatch oscillation. However, if taken account of the relatively small longitudinal filling factor (0.163) the corresponding stable region becomes $\sigma_{l0} < 92.9°$. Summarizing these two longitudinal instability constrains, the longitudinal zero current phase advances of the SC linac is designed to be started from slightly above 90°.

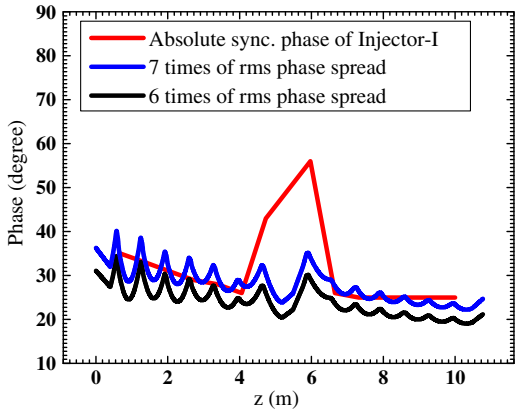

FIG. 11. The synchronous phase (absolute value) evolution (red) and 6 times (black) and 7 times (blue) of the rms phase spread evolution of the Injector I SC linac.

The accelerating gradient is limited by the longitudinal phase advance upper limit on the one hand; on the other hand by the reality that big synchronous phase has to be kept to ensure enough longitudinal acceptance. Figure 11 shows the synchronous phase (absolute value) evolution of the SC section of the Injector I linac. From the figure we can see that the synchronous phase is maintained to be bigger than 6 times of the rms phase spread.

The proton beam in ADS Injector I design is space charge dominated which fulfills the condition of $Nr_c a/\varepsilon_{nt}^2 = 461 \gg 1$. According to Eq. (2.12), the equipartitioning design could be achieved by fixing the zero current phase advance ratio of $k_{t0}L/k_{l0}L = 0.85$. Bigger transverse than longitudinal emittance out of RFQ was designed according to this condition on the intention of increasing the cavity accelerating efficiency by keeping the longitudinal phase advance approaching the upper limit. The transverse zero current phase advances of the SC linac is designed to be started from 67° accordingly. Thus the transverse beam is resonant free as the phase advance is always smaller than 90 degrees which fully filled the transverse resonant condition presented in Sec. II C (maximum around 100°). But simulation showed emittance changes in the main linac design under this condition. It was found that the reason was that the working points distributing around the equipartition line sited too close to the $k_l/k_t = 1$ stop band [22]. So that the footprints of Injector I are shifted a little away from the $k_l/k_t = 1$ stop

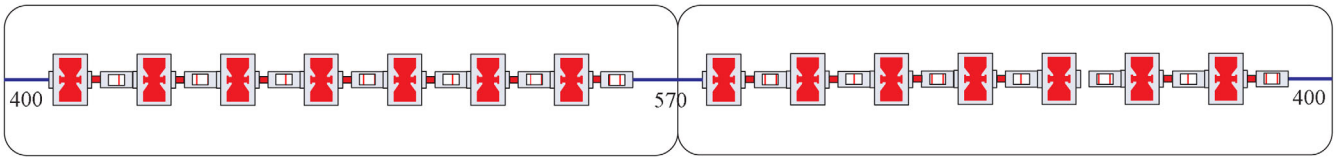

FIG. 12. Schematic of the two cryomodules layout of the Injector I SC section (unit: mm).

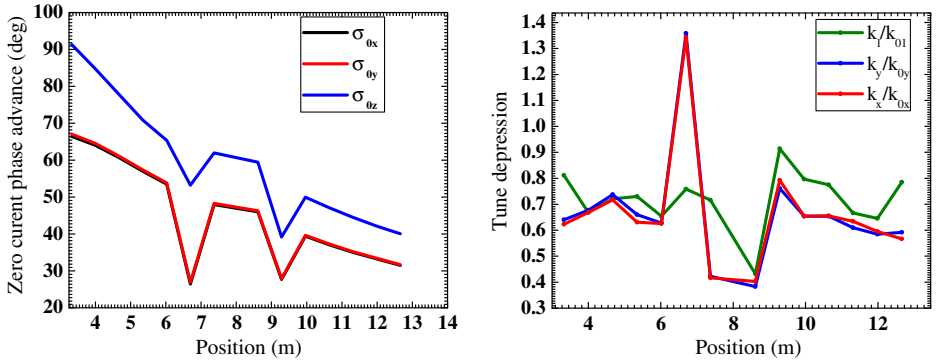

FIG. 13. Zero current phase advance of the SC section of the ADS Injector I linac (left), the tune depression along the SC section of the Injector I (right): X in red, Y in blue, and Z in green.

band by changing the zero current phase advance ratio from 0.85 to 0.75.

Previously, the SC linac of Injector I was designed to be one single cryomodule with twelve Spoke012 cavities inside. As shown in Fig. 12, in the present design, it was divided into two cryomodules (total 14 cavities) because of the common sense of the difficulties during the installation, collimation and maintenance. The distance between the two cryomodules had to be kept as short as possible, because the discontinuity of the periodical lattice brought up with the possibility of mismatch. The longer the distance is, the more difficult to get a matching solution, thus beam halo induced. In our case 570 mm is remained for the cryomodules warm to cold transition from the flange of the last cold element of the first cryomodule to the flange of the first cold element of the second cryomodule. Every effort had been made by local mechanical and beam dynamics groups to get this distance shorter for better beam performance. Originally a warm BPM between the cryomodules was planned to help the beam tuning in case the cold BPMs do not perform as expected. But it was abandoned soon after the evaluation of the space needed for the warm BPM (at least 100 mm).

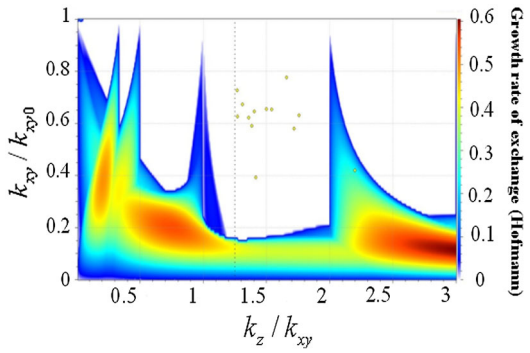

FIG. 14. Tune footprint of SC section for China ADS Injector I with $\varepsilon_{nom.rms.z}/\varepsilon_{norm.rms.t} = 0.85$

2. Beam dynamics

Beam dynamics of the Injector I SC section are carried out using the TRACEWIN [23] and DYNAC [24] programs. Figure 13 shows the designed zero current phase advance per period (left graph) and the tune depression evolution (right graph) along the SC section of the Injector I. The footprint of the Injector I SC section is shown in Fig. 14. The linac design is not equipartitioned and the working points are positioned in a relatively large region of stable area between the $k_l/k_t = 1$ and $k_l/k_t = 2$ stop bands on the Hofmann stability chart. Fixed transverse and longitudinal ratio gives smooth phase advance per meter along the linac assisting to get a good match between the two cyomodules. The only one working point overlapping with the $k_l/k_t = 2$ stop band is the sixth period used for matching. Very little emittance transfers as expected.

Figure 15 shows the RMS envelope evolution of the Injector I SC section integrated with MEBT1. The envelope is quite smooth at the transition of one cryomodule to another. RFQ simulated distribution is used in the beam dynamics with 100,000 macroparticles. The horizontal, vertical and longitudinal normalized RMS

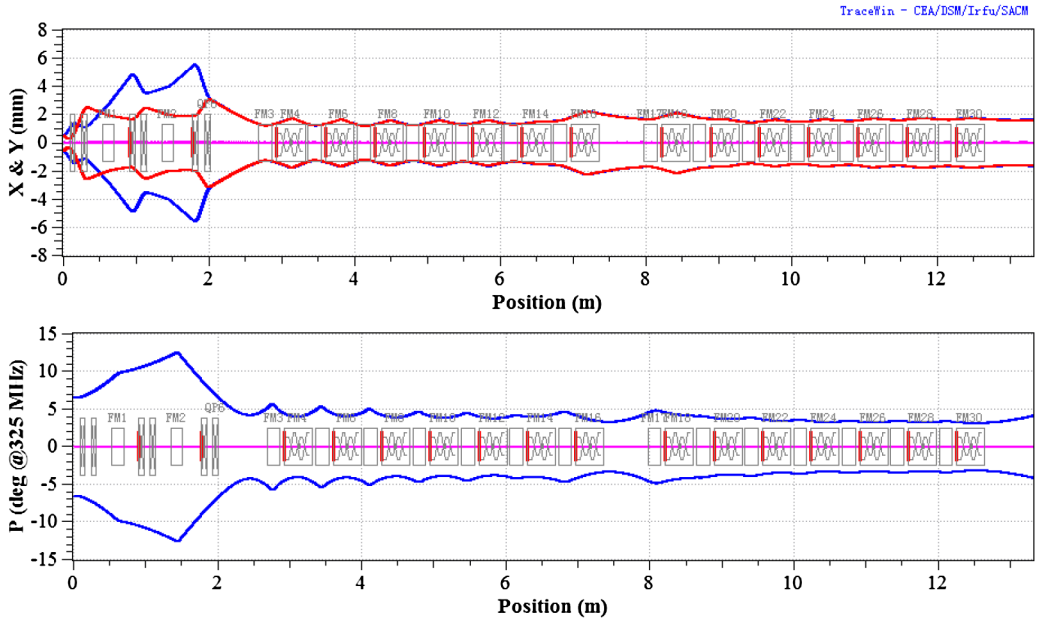

FIG. 15. The RMS envelope evolution of the Injector I SC section integrated with MEBT1.

emittance growths are 3.4%, 3.0% and 5.0% respectively from the exit of the RFQ to the end of the Injector I SC section. During the design, the normalized RMS emittance growths are considered as one major criterion for determining the matching results between the two cryomodules. In the beginning a periodical lattice was designed to be a reference using truncated 4σ and 5σ (transverse and longitudinal) Gaussian initial distribution. The normalized RMS emittance growths are 4.0%, 3.4% and 3.9% (x, y and z planes) respectively as presented in Fig. 16 (left graph). Two cryomodule designs were obtained by adding additional space between the 7th and 8th cell. After proper matching the RMS normalized emittance growths are 4.8%, 4.0% and 5.3% (x, y and z planes) respectively, as shown in Fig. 16 (right graph), around 1% growth comparing with the periodical lattice which is considered to be reasonable. Benchmarking between TRACEWIN and DYNAC is performed for the basic design of the linac from the exit of the RFQ to the end of the Injector I SC section. The simulation results of both codes are consistent. As shown in Fig. 17, the envelope and energy agree well. Emittance evolution and phase space at 10 MeV shows acceptable small deviation as shown in Fig. 17 (lower left).

Figure 18 shows the benchmarking results for the superconducting section of Injector I by TRACEWIN and DYNAC at the exit of the Injector I SC linac at 10 MeV. The field map difference employed in two codes may explain the difference. TRACEWIN code adopted 3D fields for

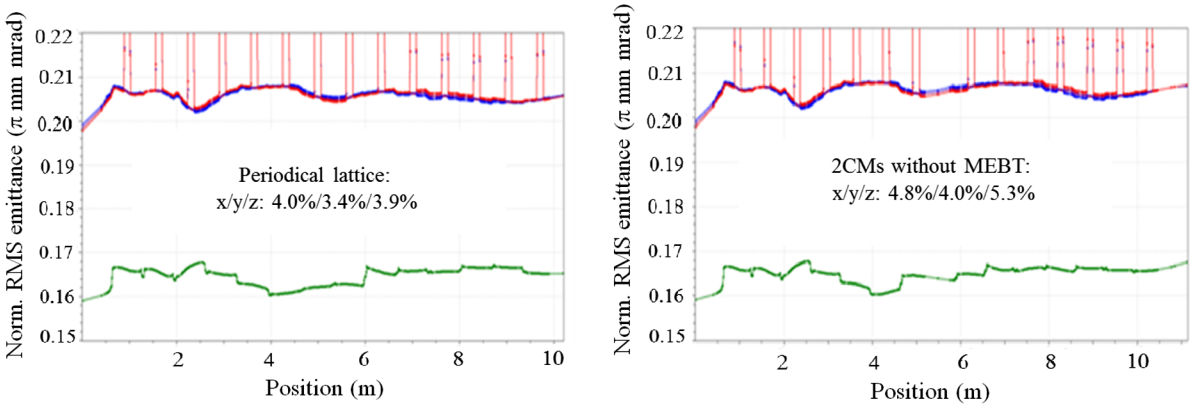

FIG. 16. The RMS envelope evolution of the Injector I SC section before (left graph: periodical lattice) and after (integrated with MEBT) separated in two cryomodules: horizontal, vertical and longitudinal are in blue, red and green respectively.

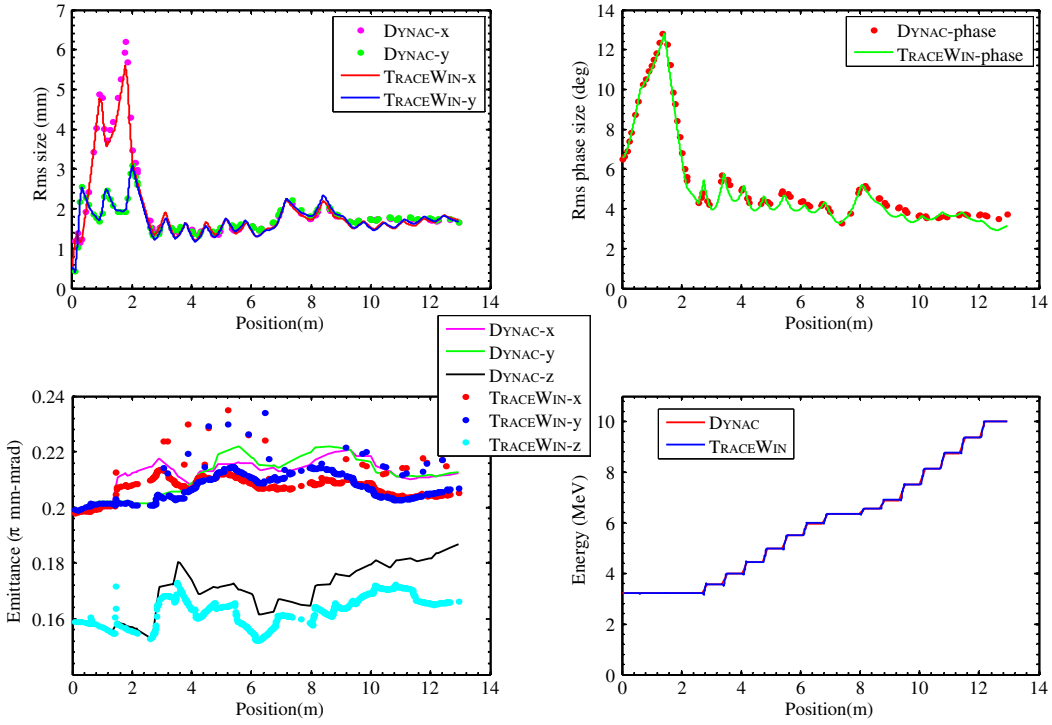

FIG. 17. The benchmarking results for the SC section of Injector I by TRACEWIN and DYNAC: the RMS transverse and longitudinal envelope, emittance and energy evolution along the SC linac.

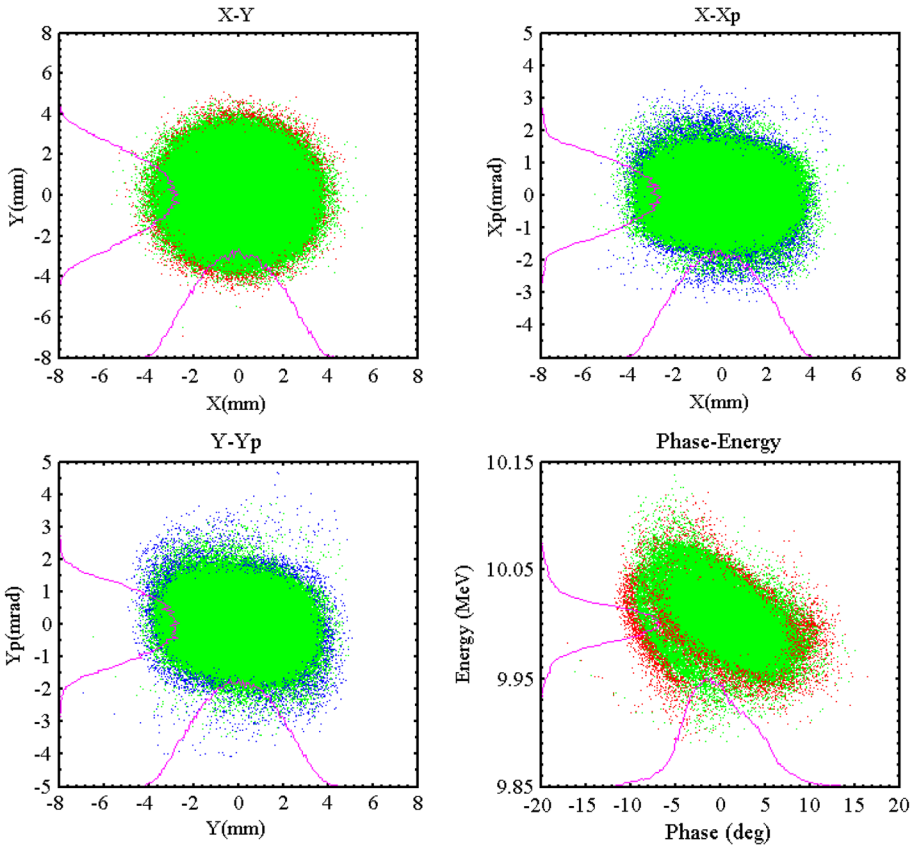

FIG. 18. The benchmarking results for the SC section of Injector I by TRACEWIN and DYNAC: the phase space @ 10 MeV.

TABLE III. The design details of the Injector I SC section start from 3.2 to 10 MeV.

Cavity Number	1	2	3	4	5	6	7	8	9	10	11	12	13	14
Synchronous phase (°)	−35	−33	−31	−29	−28	−26	−43	−56	−26	−25	−25	−25	−25	−25
E_{acc}(MV/m)	6.08	6.08	6.08	6.08	6.08	4.94	4.60	3.71	3.34	6.08	6.08	6.08	6.08	6.08

cavities and solenoids while 1D field used in DYNAC. The detail design is presented in Table III.

3. Error analysis

Radio frequency errors and misalignments setting.—The error analysis is performed on the 13.3 m long section of Injector I including MEBT1 and Spoke012 section. The goal of this paper is to verify the robustness of the SC section design. The initial input is the RFQ simulated distribution. Radio frequency errors and misalignments are considered for all the optics in this section, including buncher/cavity errors, quadrupole/solenoid misalignments and field gradient fluctuations *et al.*, as shown in Table IV. The bending magnet is a part of the beam dump line which will be introduced in Sec. III E of this paper.

The rf phase and amplitude errors of the cavities were set to ±0.5° and ±0.5% throughout the linac (RFQ errors not included). These numbers were determined according to the measured realistic results on FRIB ReA3 of MSU [25] and local domestic test results of LLRF control for 973-RFQ [26]. The peak to peak rf phase and amplitude fluctuation measured at ReA3 are ±0.2° and ±0.15% while ±0.2° and ±0.25% without beam loading and ±0.25° and ±0.35% with beam loading measured at 973-RFQ in IHEP. The rf error settings illustrated in Table IV were set to be about twice these values. The misalignments for cold optics are 1 mm and 2 mrad. Internationally 0.4 mm misalignment for cold cavity and 0.2 mm for solenoid had been achieved in TRIUMF [27] through the stretched wire alignment system (i.e., wire position monitor) which has been applied in the ADS Injector I testing facility. Alignment repeatability had been gained during the test on the TRIUMF ISAC-II linac with 0.12 mm(horizontal)/0.08 mm(vertical) [28]. The alignment standards for warm optics (0.1 mm and 2 mrad) are considered to be easily achieved by the domestic mechanical group.

A large amount of error analysis was carried out to verify the tolerance of the basic design and estimate the overall degradation of the beam properties with or without corrections using the TRACEWIN program. Initially all the errors combined simultaneously were applied as specified in Table IV. Then doubled errors were applied and all kinds of input beam errors were analyzed based on the basic design. All the errors are generated randomly and uniformly distributed between the ± maximum values. 1000 seeds are generated randomly for the error analysis of each scenario. The beam loss and emittance growth are statistically averaged over the 1000 runs and 99072 macroparticles (RFQ exit particles) in each run.

Nominal and doubled misalignment and rf errors.—Figure 19 shows the error analysis comparison with errors, corrections and without errors. The upper graphs show the transverse particle densities and the longitudinal power density with rf errors, misalignments and corrections. From the figure, we can tell that the envelope evolutions are smooth even for the halo particles, the beam is under control longitudinally and there are relatively bigger

TABLE IV. The rf errors and misalignments amplitude for the injector error analysis.

		Error amplitude					
		Buncher/cavity		Q/solenoid		B magnet	
Error type[a]		Static	Dynamic	Static	Dynamic	Static	Dynamic
Displacement	δx (mm)	0.1/1	0.002/0.01	0.1/1	0.002/0.01	0.5	0.005
	δy (mm)	0.1/1	0.002/0.01	0.1/1	0.002/0.01	0.5	0.005
Rotation	Ry (mrad)	2	0.02	2	0.02	2	0.02
	Rx (mrad)	2	0.02	2	0.02	2	0.02
	Rz (mrad)			2	0.02	2	0.02
Gradient deviation	δg(%)	0.5	0.25	0.5	0.05	0.1	0.05
rf phase	$\delta\varphi$(°)	0.5	0.25				
Longitudinal displacement	δz (mm)	0	0	0	0	0	0

[a]Note: BPM uncertainty is assumed to be 0.4 mm. All errors are uniformly distributed between the ± maximum values.

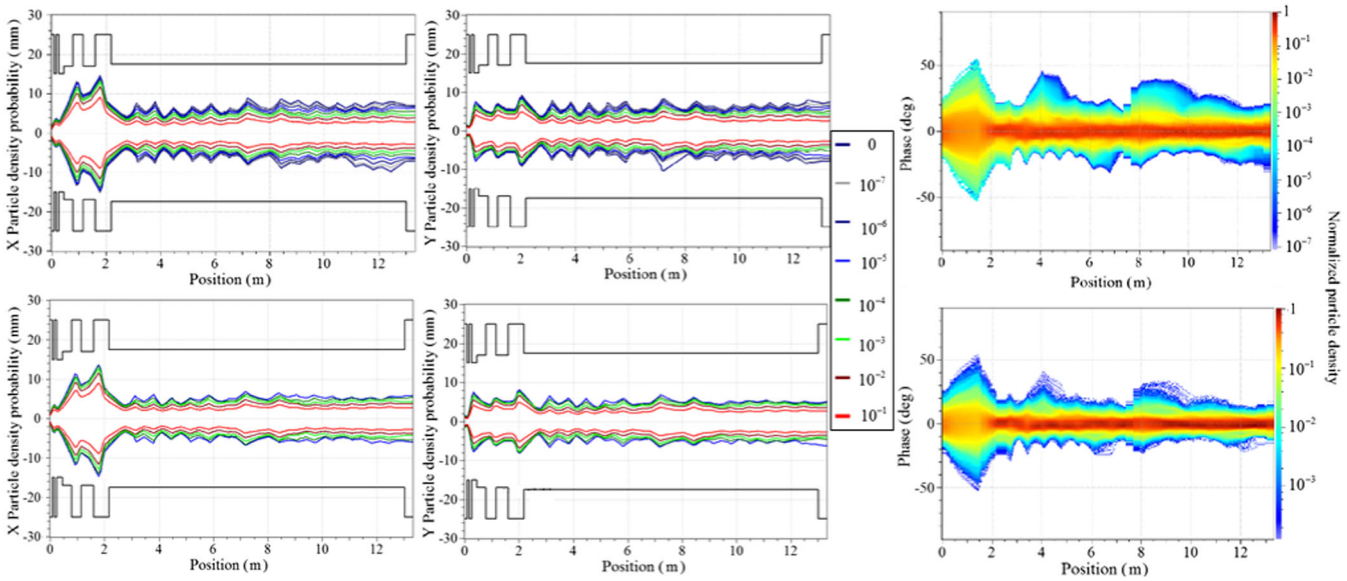

FIG. 19. The transverse particle density (graphs on the left and in the middle) and longitudinal power density (right graph) with errors, corrections (upper) and without errors (lower).

margins on transverse planes. The corresponding results without errors are shown in the lower graphs for comparing. The transverse and longitudinal normalized rms emittance growths are 5.6%, 5.2% and 9.4% respectively with errors and corrections for the basic design. If there is no correction, the corresponding horizontal, vertical and longitudinal emittance growths are 10.3%, 10.1% and 25.8%, respectively and beam losses appear as expected [see Fig. 20 (top-right graph)]. The rms residual orbit could be corrected back between 0.2 to 0.4 mm while the particle central orbit increased continuously without corrections [Fig. 20 (lower-right graph)].

Doubled errors are applied to testify the sensitivity of the beam to the errors. The beam dynamics results are presented in Fig. 21. The longitudinal tail appears and the longitudinal beam coupled to transverse at the rail of

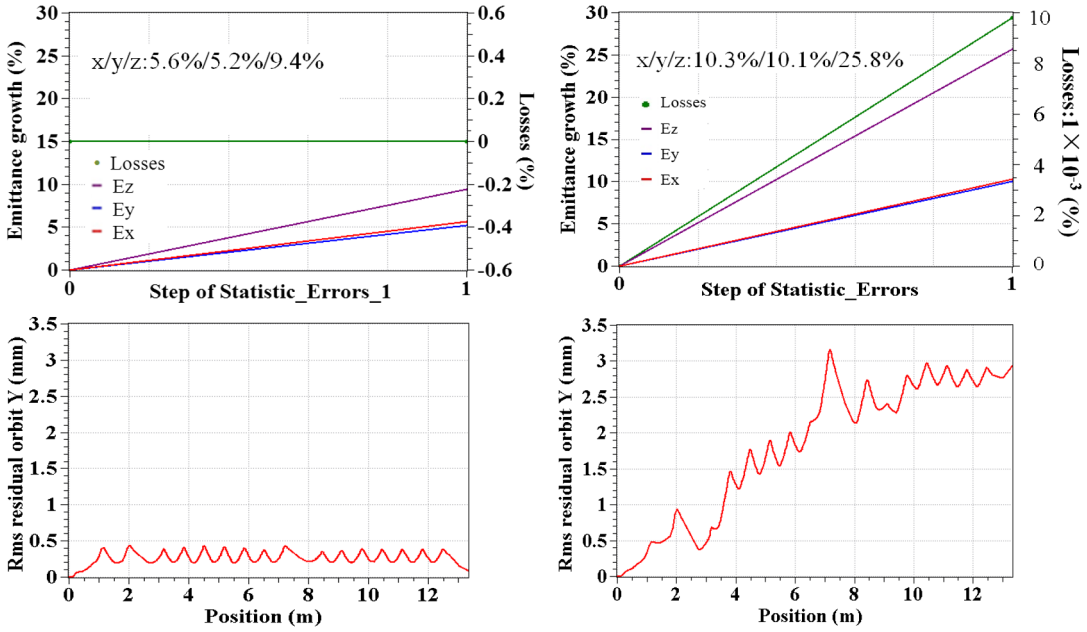

FIG. 20. The normalized RMS emittance growth and beam loss with errors and corrections (left graphs), with errors but no corrections (right figures).

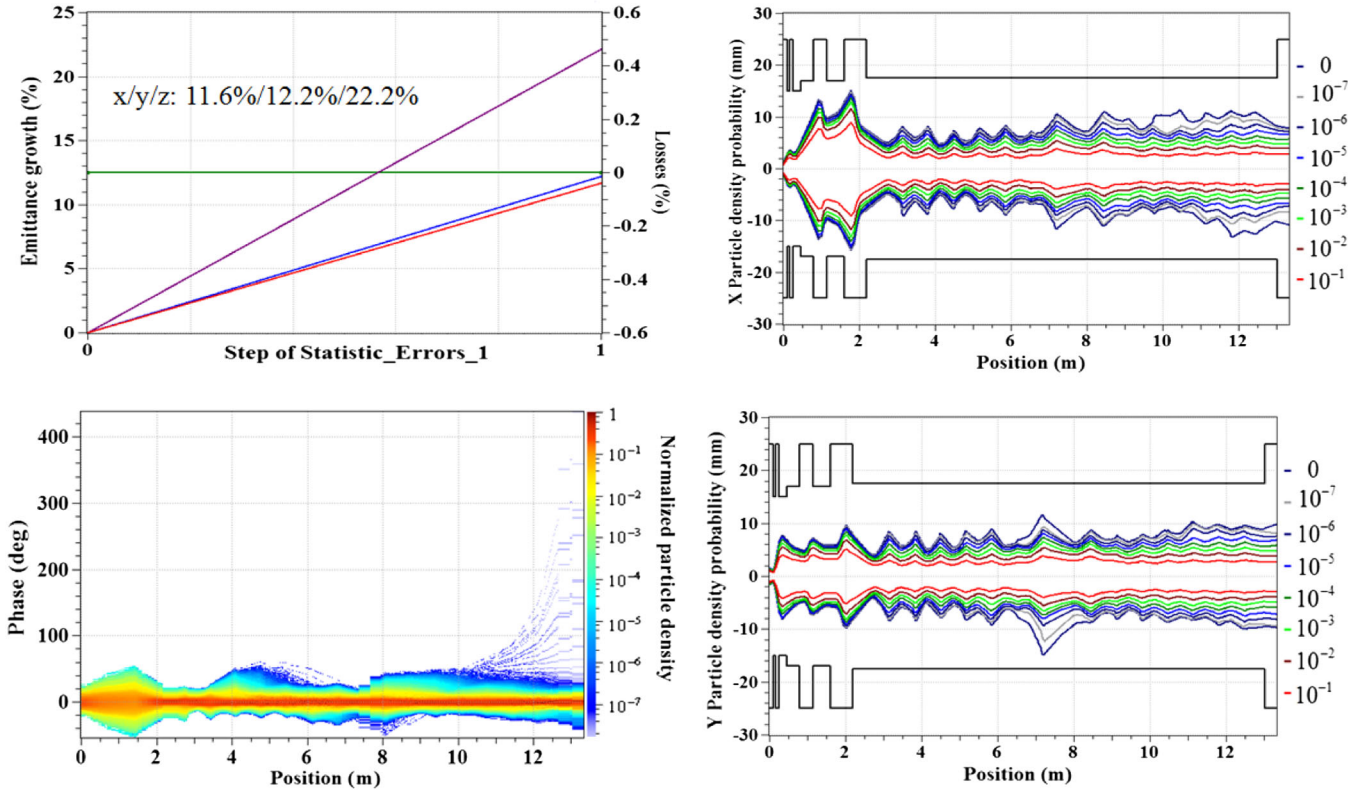

FIG. 21. The normalized rms emittance growth (left upper graph), the transverse particle density (right graphs) and longitudinal power density (lower left graph) with doubled rf errors and misalignment and corrections.

the linac. But no beam loss was observed. The normalized RMS emittance is also nearly doubled with doubled errors, which means that it is still in the linear region. Simulation results show that the beam is more sensitive longitudinally. Then rf tolerances for the cavities and bunchers (phase/amplitude: $\pm 0.5°/\pm 0.5\%$ uniform distribution) were replaced by Gaussian distributions with $\sigma = 0.5°$ in phase and $\sigma = 0.5\%$ in amplitude and truncated at $\pm 3\sigma$. The longitudinal tail appears again [similar with Fig. 21 (lower left graph)], but still no beam loss induced. The transverse and longitudinal normalized RMS emittance growths are 8.6% and 17.3% respectively. Taking the above-mentioned longitudinal Gaussian distribution errors doubled together with transverse errors, bigger longitudinal tail emerged. The tail arose from the MEBT section and grew up rapidly soon after entering into the second cryomodule, then coupled to transverse beam causing large area beam losses in the second cryomodule. The transverse and longitudinal normalized rms emittance growths are 24.1% and 65.0%. Simulations show that the situation could be improved to some extent by compressing the beam (by bunchers) before entering into the SC linac. Another effective approach is increasing the acceptance of the SC section, especially for the matching cavities at the transition segment, but the output energy will be knocked down if the overall cavity performance is not better than expected.

Input beam errors.—Five kinds of input beam errors are applied to the basic beam with all kinds of rf errors and misalignments including input mismatch/displacement/

TABLE V. The normalized RMS emittance growth and beam loss with different transverse and longitudinal input mismatches.

	Nominal	Transverse		Longitudinal		
Input mismatch (%)	0	150	200	5	10	15
Average particle loss (%)	0	0	0.0014	0	0	8×10^{-6}
Emittance growth of $\varepsilon_{norm.rms.x}$ (%)	5.6	95.9	137	5.9	6.1	6.4
Emittance growth of $\varepsilon_{norm.rms.y}$ (%)	5.2	144.8	219.8	5.0	5.1	5.1
Emittance growth of $\varepsilon_{norm.rms.z}$ (%)	9.4	45.5	44.3	11.1	14.1	27.2

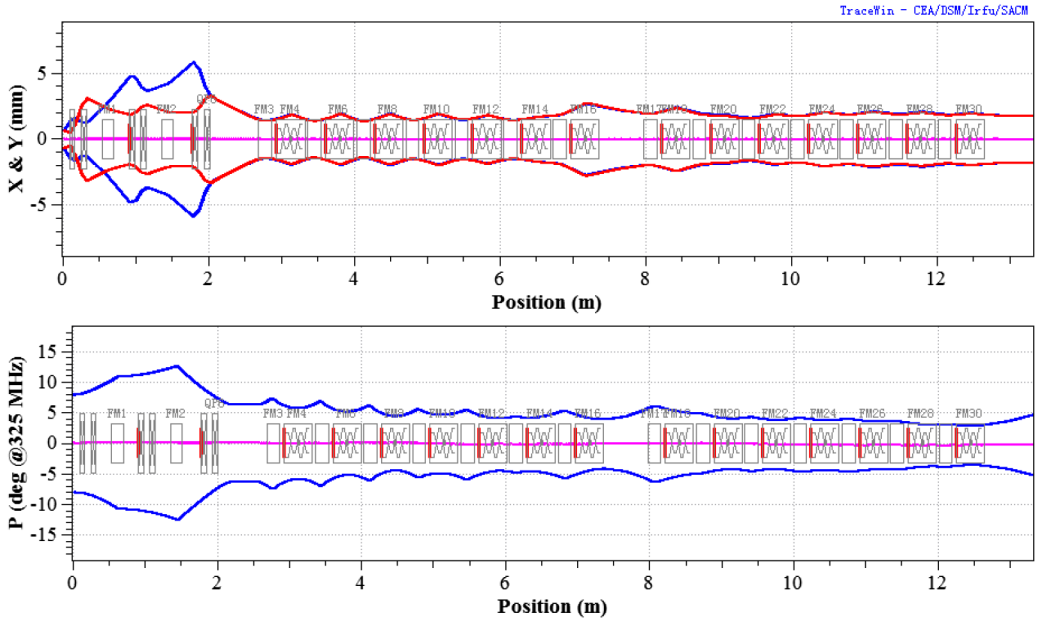

FIG. 22. The envelope evolution of the SC section of Injector I together with MEBT with 50% input emittance deviation (increasing in all three directions).

current errors and emittance deviations. Table V presents the beam dynamics results for input beam mismatches. The input beam is mismatched by a percentage, for example: a 10% mismatch in the x plane means α_x and β_x are multiplied by 1.12 (interpreted by TRACEWIN manual) while the normalized emittance remained the same. As presented in Table V, there are no beam losses until the transverse mismatch reaching 200%. But the longitudinal beam is more sensitive to the mismatch. The beam starts to lose with longitudinal mismatch of 15%. The same conclusion could be derived from the results of input beam displacements and beam current error analysis. Simulation shows that the beam has bigger tolerance to the transverse deviations. The corrector can correct the beam with input beam errors of 0.3 mm and 0.7 mrad according to the MEBT corrector design specification which is around 6.6×10^{-4} T.m (consistent with the measurements). For the longitudinal input deviations, beam starts to lose beyond the region $-2.5°$ to $2°$ in phase and -0.03 to 0.01 MeV in energy. All these results provided a reference for the limitation of the front end errors from ion source to the exit of the RFQ. Different input beam current for 0, 10, 15 and 20 mA are analyzed, no obvious changes from the basic design from 5 to 20 mA. But a big longitudinal tail emerges for the zero current case although no beam loss appears. The reason is that the matching is quite different for space charge dominated beam and zero current beam. The results show that the design has a big tolerance to the beam current deviation either. To be noted, during the analysis nothing is changed but the input beam, errors are distributed randomly and the corrector is adjusted to get the beam back to the orbit.

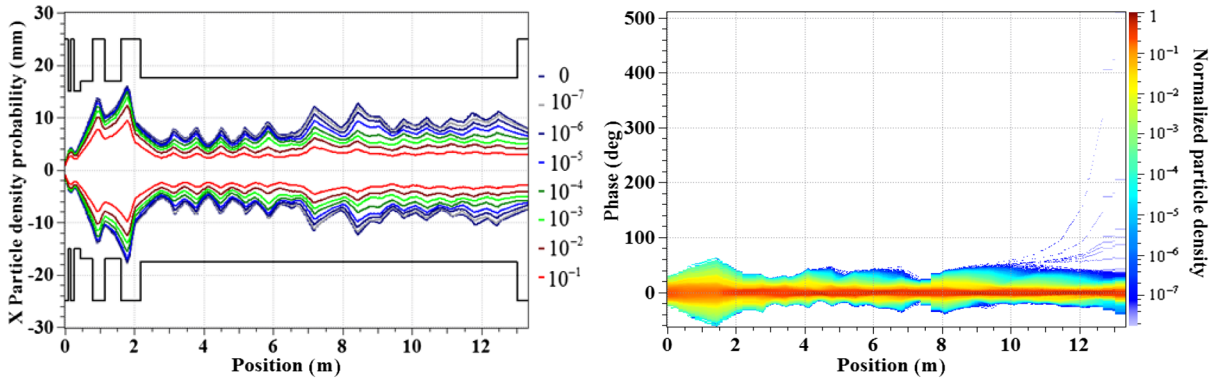

FIG. 23. The error analysis results of the 50% input emittance deviation case: transverse particle density level in the x plane (left) and longitudinal power density (right).

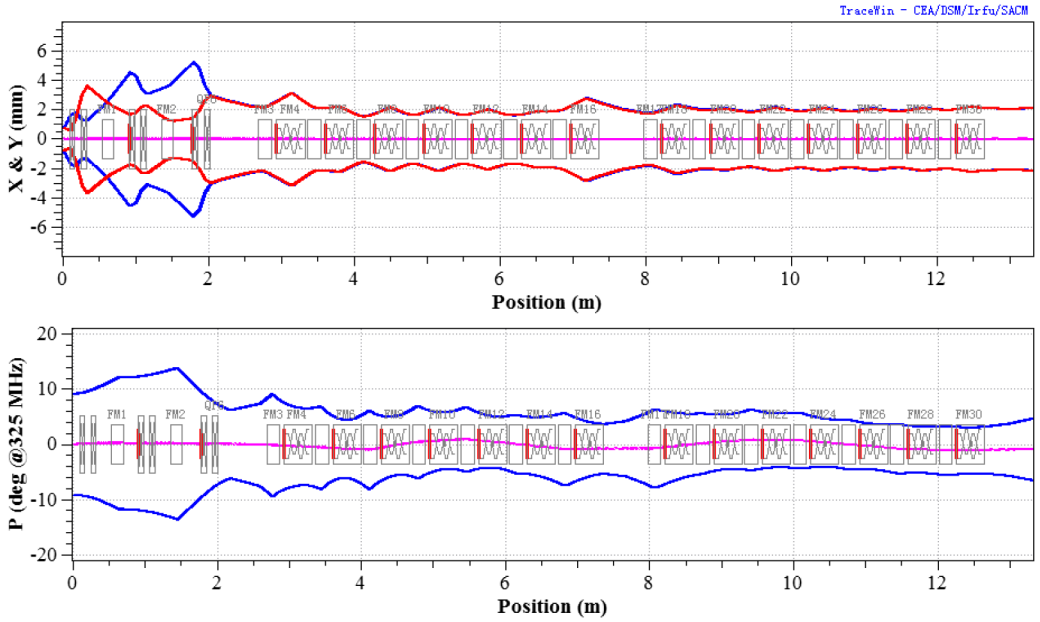

FIG. 24. The envelope evolution of the superconducting section of Injector I together with MEBT with 100% input emittance deviation (increasing in all three directions).

According to the 973-RFQ experiments, the transverse emittance deviation was 29.8% to 41.1% [29] increased up from the PARMTEQ [30] simulations. Therefore, 50% and 100% emittance deviation from the RFQ simulated results were studied to testify the flexibility of the basic design. First, emittances at the RFQ exit are increased by 50% manually in all three directions. The difficulty of this design is the longitudinal matching between RFQ to the SC linac. As the beam entering into the MEBT is 50% bigger and the MEBT bunchers cannot handle this change independently, so that the first two cells of the cryomodule one together with MEBT participated in the matching. The envelope evolution shows that the beam is quite smooth as presented in Fig. 22 and the output energy can still achieve 10 MeV. The error studies show small longitudinal tail emerging at the transition point and grows bigger at the end of the linac, but the tail is not big enough to couple into transverse yet, no beam loss appears as shown in Fig. 23.

Emittances at the RFQ exit are also increased by 100% manually in all three directions. But the first three cells of the cryomodule one together with MEBT are needed to participate in the matching. Noteworthy to reach 10 MeV, the field factor of the third Spoke012 cavity needs to be increased from 1.1 to 1.26 (corresponding to the cavity gradient increased from 6.08 to 7.0 MV/m) or all the cavity gradients increased by a smaller percentage. Although the envelope evolution is still quite smooth as shown in Fig. 24, the longitudinal beam is already entering into the nonlinear region at the second buncher position with RMS phase spread of 13.9°. Although no beam loss is observed with all rf errors, misalignments and corrections, the longitudinal tail is much bigger than 50% emittance deviation case as shown in Fig. 25.

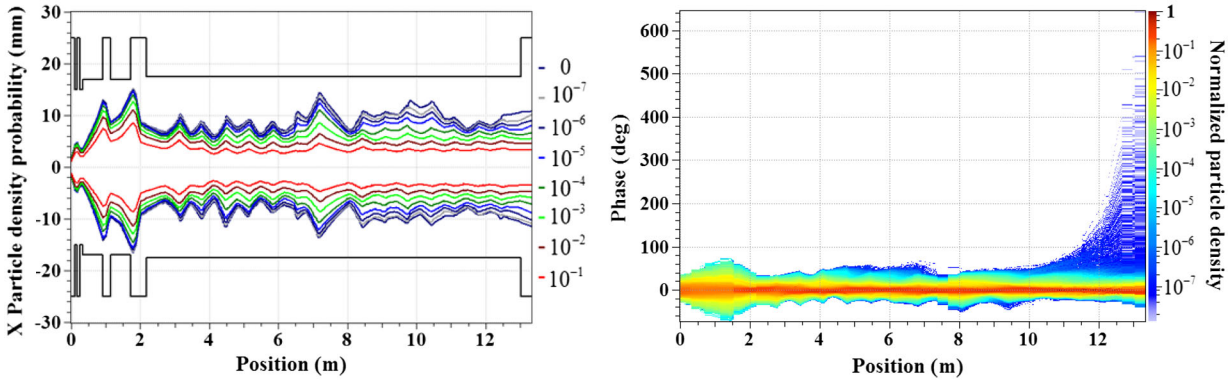

FIG. 25. The error analysis results of the 100% input emittance deviation case: transverse particle density level in the x plane (left) and longitudinal power density (right).

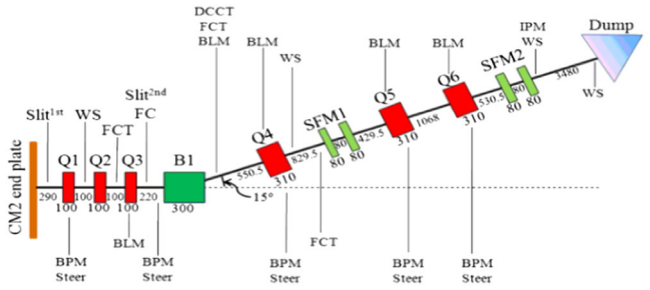

FIG. 26. The beam dump line layout of the ADS 10 MeV test stand at IHEP.

These studies give us some confidence that if there is anything out of RFQ which cannot be handled by the MEBT such as the RFQ errors or the errors from the ion source (which are not being included in this study), the SC cavities can always be involved and have the capability of completing the matching.

E. Beam dump line

The ADS 10 MeV Injector I testing facility at IHEP includes the Injector I segment and the beam dump line as shown in Fig. 2. The beam dump line is used to transport the "waste" beam from the SC section exit to the beam dump. To reduce the maximum beam power density on the beam dump target and further prolong the target life time, the step field magnets (SFM) are used to accomplish the beam transverse profile expansion and homogenization. The SFM is a newly introduced nonlinear magnet which is favored for dealing with irregular beams with dense core and sparse halo or/and with large emittance [31]. This will be the first time the SFMs are used on-line for the project. The transport beam line design and manufactures are rather difficult.

The ADS Injector I testing facility will be commissioned progressively, thus the beam dump line should be able to handle the proton beam at three different energies (i.e., 3.2, 5 and 10 MeV). The beam power density at the beam dump target is specified to be smaller than 200 W/cm^2 as per the request of the target group. The beam dump target is composed of two copper plates each having a 20° inclination angle relative to the beam direction, thus the maximum allowed transverse beam power density at the beam dump entrance should be smaller than 200 W/cm^2/sin(20°) = 585 W/cm^2. Based on the maximum beam power, the beam core size at the beam dump entrance should be at least 200 mm × 200 mm at 10 MeV, 141.4 mm × 141.4 mm at 5 MeV and 110 mm × 110 mm at 3.2 MeV. The beam loss along the beam dump line should be minimized at the most, no loss is the best. The target is designed for 100 kW applications and the same target will be used for 32 and 50 kW applications. The design principle is to limit the beam core size bigger than 200 mm × 200 mm and in the meanwhile control the halo particles within the range of 230 mm × 230 mm as much as possible. The maximum allowed rectangular beam core size is 280 mm × 280 mm.

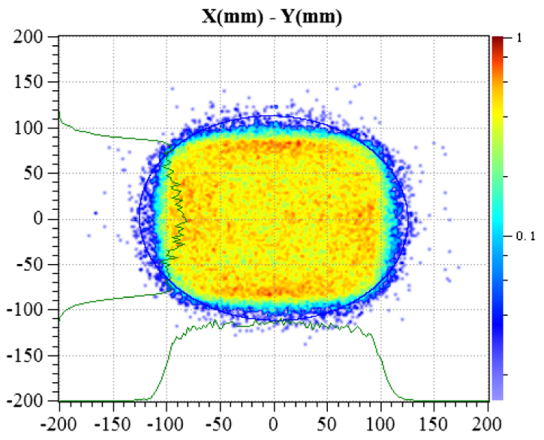

FIG. 27. Expanded and homogenized transverse beam profile at the 10 MeV beam dump entrance.

1. Lattice design

As shown in Fig. 26, the beam dump lines are composed of one bending magnet (B1), six quadruples (Q1-Q6), two pairs of SFMs (SFM1 and SFM2) and couples of beam diagnostic devices. The detailed design is presented in Ref. [32]. The lattice of the dump line for 5 and 10 MeV are completely identical and the SFM2 is moved 300 mm downstream for the 3.2 MeV. The bend angle of the magnet is designed to be 15° to avoid the recoil neutrons from the beam dump target. The total beam orbit length is 9.608 and 2.3 m in the transverse beam dump line dimension. The transverse dimension of the experiment hall is limited to be 2.5 m.

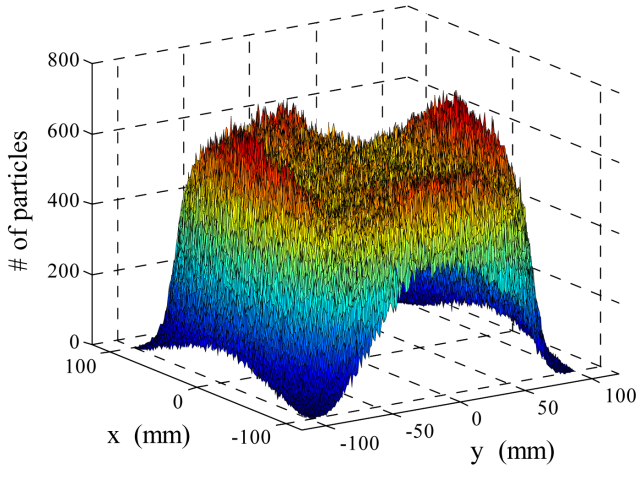

FIG. 28. Expanded and homogenized transverse particle distributions at the 10 MeV beam dump entrance with rf errors and misalignments (counted with 1 × 1 mm cell size).

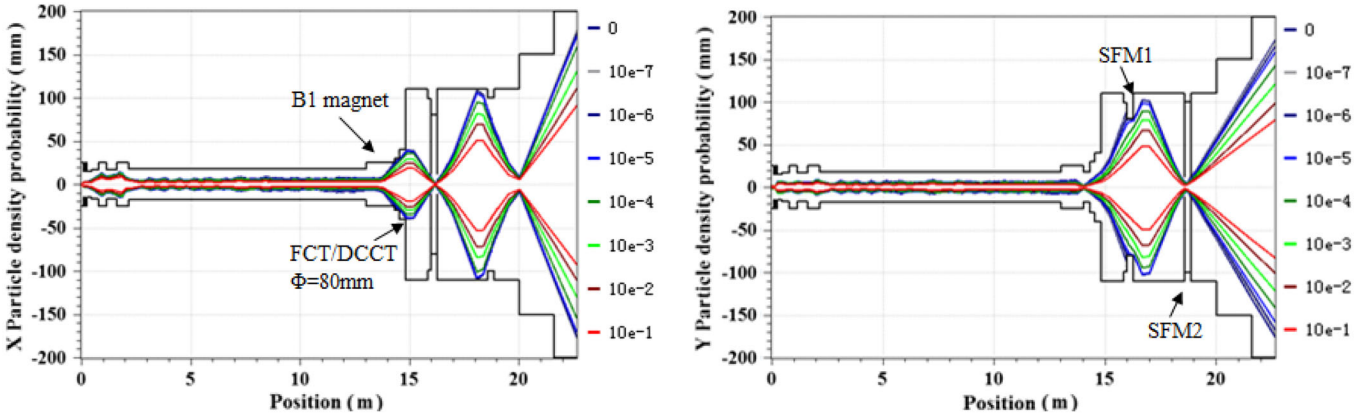

FIG. 29. The transverse particle density level with rf errors and misalignments of the Injector I test stand in the x plane (left) and the y plane (right) from the exit of RFQ to the entrance of the 10 MeV beam dump.

2. Beam dynamics and error analysis

The beam dynamics of the beam dump is integrated with MEBT and the two SC sections CM1 and CM2. As shown in Fig. 27, the transverse beam distribution at the entrance of the beam dump is designed with 90% beam within the range of 200 mm × 200 mm. Total ~4 W beam power loss is found in the positions of two pairs of SFMs for the basic design without misalignment and rf errors. Around 10 W beam power is lost along the beam dump line for the nominal misalignment and rf errors setting with beam orbit correction as shown in Fig. 29, about 2 W beam power loss in B1, ~2 W in SFM1 and ~5 W in SFM2 positions. The beam power loss distribution is in the acceptable level. To be noted, couples of optics are designed with bigger apertures as shown in Table VI to decrease the beam loss at these positions. Figure 28 shows the particle distributions at the 10 MeV beam dump entrance with rf errors and misalignments which is counted with 1 × 1 mm cell size. The maximum power density is calculated using the following equations according to the particle distribution presented in Fig. 29:

$$P_m = \frac{10\ \text{MeV} \times 10\ \text{mA} \times N_{\max}}{N_{\text{tot}} \times \text{length}_{\text{cell}} \times \text{width}_{\text{cell}}\ \text{cm}^2}, \qquad (3.1)$$

where $N_{\max} = 710$ is the maximum particle number at 1 × 1 mm cell size, N_{tot} is the total particle number in the simulation, which is 1.79×10^7 in this case. Thus the maximum power density is $P_m = 396\ \text{W/cm}^2$.

TABLE VI. Major optics aperture along the beam dump line.

Elements	Aperture: Φ (mm)
FCT & DCCT (B1 exit)	60 @3.2 MeV/80 @5&10 MeV
Q4 to Q6	220
B1 magnet	50 × 36
SFM1	24 × 160
SFM2	200 × 26

IV. SUMMARY

The paper present the physics design and the fabrication status of the ADS Injector I test stand in IHEP. The ion source and RFQ has already been installed and is under commissioning. At present, 90% duty factor had been achieved with 92% beam transmission out of the RFQ. For the SC linac, instability resonances are considered and avoided during the design in order to reduce the possible beam losses. Extensive error analyses were carried out to testify the stability of the SC linac basic design. Beam is more sensitive longitudinally and 15% mismatch at the RFQ exit will cause beam losses while the transverse mismatch upper limit is 200%. But the MEBT setting has not been readjusted in allusion to the cases with mismatches during the error anlaysis studies. The entrance mismatches accumulated in the MEBT section with all the optic errors leading to the small tolerance to the longitudinal mismatch out of the RFQ. If considering the SC section only, tolerance increases from 15% up to 75% with truncated 4σ and 5σ (transverse and longitudinal) Gaussian distribution. Although the MEBT cannot provide 100% matched beam with strong space charge as in our case, the beam mismatch factor is definitely much smaller than 75%. For the beam dump line, the SFMs are adopted for demonstrating the design scheme of the HEBT section which will transfer the 1.5 GeV proton beam with unimaginable irregular input distribution and sparse halo to the ADS transformation target. Iterative optics designs and error analysis were carried out to give a uniformed beam with beam power density on the target smaller than 585 W/cm^2. Although the beam loss is inevitable along the dump line at the positions which the beam is expanded or focused near the center of SFMs, the loss is considered to be acceptable.

ACKNOWLEDGMENTS

The authors express their sincere acknowledgment to the colleagues in the ADS accelerator team and especially the beam dynamics group for their comments, suggestions and discussions. Special thanks are expressed to Dr. XiaoYu Wu from MSU for the profit suggestions during and beyond the review. The study is supported by the CAS Strategic Priority Research Program-Future Advanced Nuclear Fission Energy (Accelerator-Driven Sub-critical System).

[1] Z. H. Li, F. Yan *et al.*, Beam dynamics of China-ADS linac, in *Proceedings of the 52nd ICPA Advanced Beam Dynamics Workshop on High-Intensity and High-Brightness Hadron Beams, HB2012, Beijing, China* (JACoW, Beijing, China, 2012).

[2] Y. He *et al.*, The conceptual design of Injector II of ADS in China, in *Proceedings of the 2nd International Particle Accelerator Conference, San Sebastián, Spain* (EPS-AG, Spain, 2011).

[3] J. Y. Tang, Z. H. Li *et al.*, IHEP-CADS-Report/2012-01 E.

[4] Z. Guo *et al.*, MEBT2 physics design for the C-ADS linac, in *Proceedings of the 52nd ICPA Advanced Beam Dynamics Workshop on High-Intensity and High-Brightness Hadron Beams, HB2012, Beijing, China* (JACoW, Beijing, China, 2012).

[5] F. Yan, Z.-H. Li, C. Meng, J.-Y. Tang, and B. Sun, Physics design for the C-ADS main linac based on two different injector design Schemes, Chin. Phys. C **38**, 027004 (2014).

[6] Z. H. Li, P. Cheng *et al.*, Physics design of an accelerator for an accelerator-driven subcritical system, Phys. Rev. ST Accel. Beams **16**, 080101 (2013).

[7] M. Reiser, *Theory and Design of Charged Particle Beams* (Wiley-VCH Verlag GmbH & Co. KGaA, Weinheim, 2008), pp. 214, 193.

[8] T. P. Wangler, *RF Linear Accelerators* (Wiley-VCH Verlag GmbH & Co. KGaA, Weinheim, 2008), pp. 332–335, 319, and references therein.

[9] Z.-H. Li, J.-Y. Tang, F. Yan, H.-P. Geng, C. Meng, B. Sun, P. Cheng, Z. Guo, and J.-L. Sun, Longitudinal instability caused by long drifts in the C-ADS injector-I, Chin. Phys. C **37**, 037005 (2013).

[10] S. M. Lund and B. Bukh, Stability properties of the transverse envelope equations describing intense ion beam transport, Phys. Rev. ST Accel. Beams **7**, 024801 (2004).

[11] M. G. Tiefenback and D. Keefe, Measurements of stability limits for a space-charge-dominated ion beam in a long A.G. transport channel, IEEE Trans. Nucl. Sci. **32**, 2483 (1985).

[12] D. Jeon, L. Groening, and G. Franchetti, Fourth order resonance of a high intensity linear accelerator, Phys. Rev. ST Accel. Beams, **12**, 054204 (2009).

[13] L. Groening, W. Barth, W. Bayer *et al.*, Experimental Evidence of Space Charge Driven Emittance Coupling in High Intensity Linear Accelerators, Phys. Rev. Lett. **102**, 234801 (2009).

[14] I. Hofmann *et al.*, Space charge resonances in two and three dimensional anisotropic beams, Phys. Rev. ST Accel. Beams **6**, 024202 (2003).

[15] M. Reiser and N. Brown, Proposed High-Current rf Linear Accelerators with Beams in Thermal Equilibrium, Phys. Rev. Lett. **74**, 1111 (1995).

[16] I. Hofmann, Stability of anisotropic beams with space charge, Phys. Rev. E **57**, 4713 (1998).

[17] Y. Yang, Z. M. Zhang *et al.*, A low energy beam transport system for proton beam, Rev. Sci. Instrum. **84**, 033306 (2013).

[18] Y. Yang, *China ADS international review, 2013, Bejing, China*, p. 7; Y. He, *China ADS mid-term report, 2013, IMP, Lanzhou, China*, p. 23.

[19] S. N. Fu, S. X. Fang, and J. Wei, China spallation neutron source linac design, in *Proceedings of the 23rd International Linac Conference, LINAC-2006, Knoxville, TN, 2006* (JACoW, Knoxville, TN, 2006), pp. 165–167.

[20] Internal beam tuning report of China ADS front end from the ion source to the exit of RFQ.

[21] Y. L. Chi *et al.*, Progress of injector-I and main linac of Chinese ADS proton accelerator, in *Proceedings of the 4th International Particle Accelerator Conference, IPAC-2013, Shanghai, China, 2013* (JACoW, Shanghai, China, 2013).

[22] F. Yan, Z. H. Li, and J. Y. Tang, Preliminary physics design of China Accelerator Driven Sub-critical System main linac, High Power Laser and Particle Beams **25**, 1783 (2013).

[23] http://irfu.cea.fr/Sacm/logiciels/index3.php.

[24] P. Lapostolle, F. Meot, and S. Valero, A new dynamics code DYNAC for electrons, protons and heavy ions in linacs with long accelerating elements, in *Proceedings of the 1990 Linear Accelerator Conference, Albuquerque, New Mexico, USA* (JACoW, Albuquerque, New Mexico, USA, 1990).

[25] X. Wu, *Accelerating physics R&D for the superconducting linac projects at Michigan State University, visiting report in IHEP, 2013*.

[26] Internal news report on IHEP website at 2012.06.26: http://acc1.ihep.ac.cn/hdxw/06/338152.shtml.

[27] R. E. Laxdal *et al.*, Cryogenic, magnetic and rf performance of the ISAC-II medium beta crymodule at TRIUMF, in *Proceedings of the 21st Particle Accelerator Conference, Knoxville, TN, 2005* (IEEE, Piscataway, NJ, 2005).

[28] I. Sekachev, *ISAC-II SC-linac cryogenic system at TRIUMF, Cryogenics Operations Workshop 2006, Stanford, California* [http://www.slac.stanford.edu/econf/C0605091/present/SEKACHEV.PDF].

[29] H. P. Jiang, S. N. Fu *et al.*, Characterizing a proton beam with two different methods in beam halo experiments, Chin. Phys. C **38**, 087002 (2014).

[30] http://laacg.lanl.gov/laacg/services/serv_codes.phtml.

[31] J. Y. Tang, H. H. Li, S. Z. An, and R. Maier, Distribution transformation by using step-like nonlinear magnets, Nucl. Instrum. Methods Phys. Res., Sect. A **532**, 538 (2004), and references therein.

[32] Z. Yang *et al.*, Transverse profile expansion and homogenization at target for the injector scheme-I test stand of China-ADS, Chin. Phys. C **39**, 027001 (2015).